Well-Balanced Central Schemes on Overlapping Cells with Constant Subtraction Techniques for the Saint-Venant Shallow Water System

Suo Yang [†], Alexander Kurganov [‡], Yingjie Liu [§]

Abstract

We develop well-balanced finite-volume central schemes on overlapping cells for the Saint-Venant shallow water system and its variants. The main challenge in deriving the schemes is related to the fact that the Saint-Venant system contains a geometric source term due to nonflat bottom topography and therefore a delicate balance between the flux gradients and source terms has to be preserved. We propose a constant subtraction technique, which helps one to ensure a well-balanced property of the schemes, while maintaining arbitrary high-order of accuracy. Hierarchical reconstruction limiting procedure is applied to eliminate spurious oscillations without using characteristic decomposition. Extensive one- and two-dimensional numerical simulations are conducted to verify the well-balanced property, high-order of accuracy, and non-oscillatory high-resolution for both smooth and nonsmooth solutions.

1 Introduction

The Saint-Venant system [8] is one of the most commonly used models of shallow water flows in rivers or coastal areas. Let h represent the water depth, u represent the velocity, B represent the bottom elevation, and g be the gravitational acceleration constant. Then the one-dimensional (1-D) Saint-Venant shallow water system has the following form:

$$\begin{cases} h_t + (hu)_x = 0, \\ (hu)_t + \left(hu^2 + \dfrac{1}{2}gh^2\right)_x = -ghB_x. \end{cases} \tag{1.1}$$

Similarly, let u and v represent the x- and y-velocities. Then the two-dimensional (2-D) Saint-

[†]School of Mathematics, Georgia Institute of Technology, Atlanta, GA 30332; syang305@gatech.edu. Research supported in part by NSF grant DMS-1115671.

[‡]Mathematics Department, Tulane University, New Orleans, LA 70118; kurganov@math.tulane.edu. Research supported in part by NSF grant DMS-1216957 and ONR grant N00014-12-1-0833.

[§]School of Mathematics, Georgia Institute of Technology, Atlanta, GA 30332; yingjie@math.gatech.edu. Research supported in part by NSF grant DMS-1115671.

Venant shallow water system reads

$$\begin{cases} h_t + (hu)_x + (hv)_y = 0, \\ (hu)_t + \left(hu^2 + \frac{1}{2}gh^2\right)_x + (huv)_y = -ghB_x, \\ (hv)_t + (huv)_x + \left(hv^2 + \frac{1}{2}gh^2\right)_y = -ghB_y. \end{cases} \tag{1.2}$$

The viscous effects were neglected by asymptotic analysis in the derivation of the Saint-Venant system [8], and therefore, in the case of flat bottom topography ($B_x \equiv B_y \equiv 0$), its behavior and features are very similar to the Euler equations of isentropic gas dynamics. For situations like dam breaking, strong shocks can be formed just like in the isentropic gas dynamics. For these reasons, high-resolution non-oscillatory shock-capturing schemes are required to solve the Saint-Venant system, which in the case of nonflat bottom topography is a hyperbolic system of balance laws. In principle, all numerical schemes designed for hyperbolic conservation laws can be extended to balance laws. This motivates us to study applicability of finite-volume central schemes on overlapping cells (CSOC), originally developed for hyperbolic systems of conservation laws in [18–20], to the shallow water equations.

In the past three decades, many numerical methods for the Saint-Venant system have been proposed. Just like many other systems of balance laws, the Saint-Venant system admits steady-state solution, in which the flux gradient is exactly balanced by the source term. The simplest steady-state solutions are "lake at rest" ones. In the 1-D case, they are

$$w := h + B \equiv \text{Const}, \qquad u \equiv 0,$$

where w represents the water surface. Similarly, the 2-D "lake at rest" satisfies

$$w \equiv \text{Const}, \qquad u \equiv v \equiv 0. \tag{1.3}$$

The "lake at rest" solutions are physically significant since most of physically relevant water waves are in fact small perturbations of "lake at rest" steady states. We therefore say that a scheme is well-balanced if it is capable of exactly preserving "lake at rest" steady states. Unfortunately, a straightforward discretization of the geometric source term typically leads to a non-well-balanced scheme, which may produce artificial waves that are an order of magnitude larger than the physical waves especially when a coarse grid is used (which is always the case in practical applications in which using sufficiently fine grids is typically unaffordable).

A second-order accurate quasi-steady wave-propagation scheme was proposed in [17]. In this scheme, a new Riemann problem is introduced at the centroid of each cell such that the flux difference can exactly cancel the contribution of the source term. A Riemann-problem-solver-free central-upwind scheme was proposed in [15, 16]. In this scheme, w rather than h is used in the reconstruction step to keep equilibrium variables constant and the numerical flux term can be approximated with high-order accuracy, while the source term is only second-order accurate to preserve the well-balanced property. A higher-order discretization of the source term was proposed in [23, 24]. Another approach was introduced in [36–38], where high-order well-balanced finite-difference and finite-volume weighted essentially non-oscillatory (WENO) schemes as well as discontinuous Galerkin methods were derived using a special local splitting of the source term for which all operators are linear and thus the well-balanced property can be easily achieved. For

several other well-balanced schemes for the Saint-Venant system we refer the reader to [2, 10, 14, 21, 25].

In this paper, we develop finite-volume CSOC with the hierarchical reconstruction (HR) limiter [18–20] for both the 1-D and 2-D Saint-Venant systems. Just like the schemes in [36–38], our scheme can also be formulated to achieve arbitrary high-order while still preserving well-balanced property using the constant subtraction technique, which is substantially easier to implement than the well-balancing techniques used in [36–38]. Another attractive feature of the proposed finite-volume CSOC is that no (approximate) Riemann problem solver needs to be implemented and all significant spurious oscillations can be removed by the HR limiter implemented together with a new remainder correction technique without local characteristic decomposition.

This paper is organized as follows. In Section 2, we briefly review the finite-volume CSOC for general hyperbolic systems of balance laws. In Section 3, we propose the constant subtraction technique and prove that it leads to well-balanced schemes. In Section 4, we review the HR limiters and develop the remainder correction technique. Extensive numerical simulations are conducted in Sections 5 and 6 for the 1-D and 2-D Saint-Venant systems, respectively. Finally, conclusions and perspectives of the future work are given in Section 7.

2 Finite-Volume Central Schemes on Overlapping Cells—A Brief Overview

A general 1-D hyperbolic system of balance laws has the following form:

$$\boldsymbol{u}_t + \boldsymbol{f}(\boldsymbol{u})_x = \boldsymbol{S}(\boldsymbol{u}, x, t). \tag{2.1}$$

Let $D_{i+\frac{1}{2}} := [x_i, x_{i+1}]$ be a cell of uniform ($x_{i+1} - x_i \equiv \Delta x$) partition of the real line, and let $\overline{\boldsymbol{V}}^n_{i+\frac{1}{2}}$ be the corresponding computed cell averages of $\boldsymbol{u}$ at time t^n:

$$\overline{\boldsymbol{V}}^n_{i+\frac{1}{2}} :\approx \frac{1}{\Delta x}\int\limits_{x_i}^{x_{i+1}} \boldsymbol{u}(x, t^n)\,dx.$$

Let $C_i := [x_{i-\frac{1}{2}}, x_{i+\frac{1}{2}}]$ be a dual cell of staggered uniform partition, and let $\overline{\boldsymbol{U}}^n_i$ be the corresponding computed cell averages of $\boldsymbol{u}$ at time t^n:

$$\overline{\boldsymbol{U}}^n_i :\approx \frac{1}{\Delta x}\int\limits_{x_{i-\frac{1}{2}}}^{x_{i+\frac{1}{2}}} \boldsymbol{u}(x, t^n)\,dx.$$

We can now apply CSOC from [18–20] to (2.1) to get the following fully discrete form (for conciseness, we will only show the updating formula for $\{\overline{\boldsymbol{V}}_{i+\frac{1}{2}}\}$, the formula for $\{\overline{\boldsymbol{U}}_i\}$ is similar):

$$\begin{aligned}\overline{\boldsymbol{V}}^{n+1}_{i+\frac{1}{2}} = {}& \theta\frac{1}{\Delta x}\int\limits_{x_i}^{x_{i+1}} \widetilde{\boldsymbol{U}}^n(x)\,dx + (1-\theta)\overline{\boldsymbol{V}}^n_{i+\frac{1}{2}} - \frac{\Delta t}{\Delta x}\big[\boldsymbol{f}(\widetilde{\boldsymbol{U}}^n(x_{i+1})) - \boldsymbol{f}(\widetilde{\boldsymbol{U}}^n(x_i))\big] \\ & + \frac{\Delta t}{\Delta x}\int\limits_{x_i}^{x_{i+1}} \boldsymbol{S}(\widetilde{\boldsymbol{U}}^n(x), x, t^n)\,dx.\end{aligned} \tag{2.2}$$

Here, $\widetilde{\boldsymbol{U}}$ is the reconstructed piecewise polynomial approximation of $\boldsymbol{u}(x,t^n)$, and $\theta=\Delta t/\Delta\tau$, where $\Delta\tau$ is an upper bound for the current time stepsize Δt. $\Delta\tau$ is restricted by the CFL condition $\frac{a\Delta\tau}{\Delta x}\le\frac{1}{2}$, where a is the supremum of the spectral radius of the Jacobian $\frac{\partial\boldsymbol{f}}{\partial\boldsymbol{u}}$ over all of the relevant values of $\boldsymbol{u}$. Also notice that CSOC with $\theta=1$ is a first-order in time version of the (staggered) Nessyahu-Tadmor scheme [22]. For pure hyperbolic systems, θ in principle should be as large as possible to allow large Δt and hence reduce the computational cost. When the source term is stiff, one can also take a smaller value of θ.

If we subtract $\overline{\boldsymbol{V}}^n_{i+\frac{1}{2}}$ from both sides of (2.2), divide by Δt, and take the limit as $\Delta t\to 0$, we obtain the following semi-discrete form of the finite-volune CSOC:

$$\frac{d}{dt}\overline{\boldsymbol{V}}_{i+\frac{1}{2}}=\frac{1}{\Delta\tau}\left[\frac{1}{\Delta x}\int\limits_{x_i}^{x_{i+1}}\widetilde{\boldsymbol{U}}(x)\,dx-\overline{\boldsymbol{V}}_{i+\frac{1}{2}}\right]-\frac{1}{\Delta x}\Big[\boldsymbol{f}(\widetilde{\boldsymbol{U}}(x_{i+1}))-\boldsymbol{f}(\widetilde{U}(x_i))\Big]+\frac{1}{\Delta x}\int\limits_{x_i}^{x_{i+1}}\boldsymbol{S}(\widetilde{\boldsymbol{U}}(x),x,t)dx. \tag{2.3}$$

One should use a stable, sufficiently accurate ODE solver to evolve the solution in time.

Remark 2.1 In our numerical experiments, we have used the third-order strong-stability preserving Runge-Kutta (SSP-RK3) method [11, 12, 29].

Remark 2.2 Multidimensional finite-volume CSOC can be derived similarly, see [18].

3 Constant Subtraction Technique

Our goal is to design well-balanced CSOC. We first consider the 1-D case and denote the equilibrium variables by $\boldsymbol{a}:=(w,hu)^T$, which remains constant at "lake at rest" steady states. Next, we rewrite the geometric source term using the equilibrium variable w as follows:

$$-ghB_x=-g(w-B)B_x=\left(\frac{1}{2}gB^2\right)_x-gwB_x, \tag{3.1}$$

where the term $(\frac{1}{2}gB^2)_x$ is in conservative form.

Remark 3.1 Notice that the same source term decomposition was used in [36] to maintain a well-balanced property of arbitrary high-order finite-difference schemes.

Since a direct application of the CSOC to the Saint-Venant system (1.1) does not guarantee the resulting method to be well-balanced, we modify the system and obtain the well-balanced CSOC using the following algorithm.

Algorithm 3.1 (Constant Subtraction Technique)

Step 1. Let Ω be a computational domain of size $|\Omega|$. Denote the global spatial average of $w(x,t)$ by

$$\overline{w}(t):=\frac{1}{|\Omega|}\int\limits_{\Omega}w(x,t)\,dx$$

and decompose the nonconservative term on the right-hand side (RHS) of (3.1) into the sum of a conservative term and a *constant subtraction term* as follows:

$$-gwB_x=(-g\bar{w}B)_x+g(\bar{w}-w)B_x. \tag{3.2}$$

Step 2. Use (3.1) and (3.2) to rewrite the Saint-Venant system (1.1) in terms of the equilibrium variables $\boldsymbol{a}$:

$$\begin{cases} w_t + (hu)_x = 0, \\ (hu)_t + \left(\dfrac{(hu)^2}{w-B} + g[\overline{w}(t) - w]B + \dfrac{g}{2}w^2\right)_x = g[\overline{w}(t) - w]B_x. \end{cases} \tag{3.3}$$

Step 3. Apply the CSOC described in Section 2 to the system (3.3) in a straightforward manner.

Remark 3.2 The systems (3.3) and (1.1) are equivalent for both smooth and nonsmooth solutions.

Remark 3.3 The term $g[\overline{w}(t) - w]B_x$ will vanish at "lake at rest" steady states.

Theorem 3.1 *The CSOC scheme with the forward Euler time discretization* (2.2) *for the system* (3.3) *is well-balanced.*

Proof: Note that at "lake at rest" steady states $\overline{w}(t)$ is independent of time and assume that at time $t = t^n$ the cell averages of $\boldsymbol{a}$ over both C_i and $D_{i+1/2}$ cells are equal to $(\overline{w}, 0)^T$. After performing a (high-order) piecewise polynomial reconstruction for the equilibrium variables $\boldsymbol{a}$, we obtain that the polynomial pieces over both C_i and $D_{i+1/2}$ still satisfy $\widetilde{hu} \equiv 0$ and $\widetilde{w} \equiv \overline{w}$. Therefore, both the flux difference and source term in the CSOC (2.2) vanish and $\overline{\boldsymbol{V}}^{n+1}_{i+\frac{1}{2}}$ becomes a convex combination of $\frac{1}{\Delta x}\int_{x_i}^{x_{i+1}} \widetilde{\boldsymbol{U}}^n(x)\,dx$ and $\overline{\boldsymbol{V}}^{n}_{i+\frac{1}{2}}$, both of which are at "lake at rest" steady state. Therefore, the cell averages at $t = t^{n+1}$ also satisfy $hu = 0$ and $w = \overline{w}$ and the proof of the theorem is complete. ■

Remark 3.4 We would like to stress that in order to guarantee the well-balanced property, it is important to reconstruct the equilibrium variables $\boldsymbol{a}$ rather than the original ones, $(h, hu)^T$.

Remark 3.5 Since SSP ODE solvers [11, 12, 29] are based on a convex combination of several forward Euler steps, Theorem 3.1 is valid for the semi-discrete CSOC (2.3) combined with a higher-order SSP solver.

Remark 3.6 All of the results from Section 3 can be directly extended to the 2-D case.

Remark 3.7 In this paper, we design the scheme that preserves "lake at rest" steady states $h + B = C$ and $u = 0$, for which C is a constant in the entire computational domain. This steady state has substantial practical importance. For more complicated situations, for example, if we have two parts of the domain connected by a river system. Then, the "lake at rest" steady states on the left and on the right may be at different water surface levels and averaging them over the entire computational domain will not make any sense. One will probably have to use a domain decomposition technique to design the CSOC scheme that would preserve such steady states. This type of study goes beyond the scope of our paper.

4 Non-Oscillatory Hierarchical Reconstruction (HR)

For discontinuous solutions, a nonlinear limiting procedure is typically required to eliminate spurious oscillations in the vicinities of discontinuities. In the past few decades, a wide variety of nonlinear limiting techniques including the MUSCL [31–33], ENO [13, 26, 29, 30] and WENO [27, 28] reconstructions and many others have been developed for solving this problem. In this paper, we use the HR limiting technique originally designed in [19, 20] for overlapping grid methods.

4.1 HR Process—A Brief Overview

Let us assume that we are given a set of cell averages, $\overline{\varphi}_i$ and $\overline{\varphi}_{i+\frac{1}{2}}$, of a certain computed quantity on overlapping cells. Then, using a standard conservation technique one can build a central piecewise polynomial reconstruction of degree d on each cell (see, e.g., [20]). Unfortunately, a piecewise polynomial approximant reconstructed in such a linear, nonlimited way may have spurious oscillations in nonsmooth regions and thus it must be corrected using a nonlinear limiter.

Suppose we have reconstructed polynomial pieces over the overlapping cells C_i and $D_{i+\frac{1}{2}}$, $\varphi_i(x)=\sum\limits_{m=0}^{d}\frac{\varphi_i^{(m)}(x_i)}{m!}(x-x_i)^m$ and $\varphi_{i+\frac{1}{2}}(x)=\sum\limits_{m=0}^{d}\frac{\varphi_{i+\frac{1}{2}}^{(m)}(x_{i+\frac{1}{2}})}{m!}(x-x_{i+\frac{1}{2}})^m$, expressed in terms of Taylor polynomials centered at x_i and $x_{i+\frac{1}{2}}$, respectively. We now describe the HR process applied to $\varphi_i(x)$ (an application of the HR to $\varphi_{i+\frac{1}{2}}(x)$ is similar). Using the HR to limit the polynomial $\varphi_i(x)$ is to modify its coefficients $\varphi_i^{(m)}(x_i)$ to obtain their new values $\widetilde{\varphi}_i^{(m)}(x_i)$, thus generating a non-oscillatory polynomial $\widetilde{\varphi}_i(x)$ with the same order of accuracy. In the following, we use a pointwise HR proposed in [39] to explain the 1-D HR algorithm.

Algorithm 4.1 (Pointwise HR)

Step 1. Suppose $d\geq 2$. Then, for $m=d,d-1,\cdots,1$ do the following:

(a) Take the $(m-1)$th derivatives of φ_i and $\varphi_{i\pm\frac{1}{2}}$ and write $\varphi_i^{(m-1)}(x)=L_{m,i}(x)+R_{m,i}(x)$, where $L_{m,i}(x)$ is the linear part and $R_{m,i}(x)$ is the remainder.

(b) Compute the cell average of $\varphi_i^{(m-1)}$ over C_i to obtain the cell average $\overline{\varphi_i^{(m-1)}}$. Also compute the point values $\varphi_{i+\frac{1}{2}}^{(m-1)}(x_{i+\frac{1}{2}})$ and $\varphi_{i-\frac{1}{2}}^{(m-1)}(x_{i-\frac{1}{2}})$.

(c) Let $\widetilde{R}_{m,i}(x)$ be $R_{m,i}(x)$ with its coefficients replaced by the corresponding modified values. Compute the cell average of $\widetilde{R}_{m,i}$ over C_i to obtain the cell average $\overline{\widetilde{R}_{m,i}}$. Also compute the point values $\widetilde{R}_{m,i}(x_{i+\frac{1}{2}})$ and $\widetilde{R}_{m,i}(x_{i-\frac{1}{2}})$.

(d) Let $\overline{L}_{m,i}:=\overline{\varphi_i^{(m-1)}}-\overline{\widetilde{R}_{m,i}}$ and $\overline{L}_{m,i\pm\frac{1}{2}}:=\varphi_{i\pm\frac{1}{2}}^{(m-1)}(x_{i\pm\frac{1}{2}})-\widetilde{R}_{m,i}(x_{i\pm\frac{1}{2}})$.

(e) Reconstruct a non-oscillatory linear function $L(x)$ on C_i using $\overline{L}_{m,i}$, $\overline{L}_{m,i+\frac{1}{2}}$ and $\overline{L}_{m,i-\frac{1}{2}}$, and define the modified coefficient $\widetilde{\varphi}_i^{(m)}(x_i):=L'(x)$.

Step 2. The modified 0th degree coefficient $\widetilde{\varphi}_i(x_i)$ is chosen such that the cell average of $\widetilde{\varphi}_i(x)$ over C_i is equal to $\overline{\varphi}_i$.

After the set of modified coefficients $\widetilde{\varphi}_i^{(m)}(x_i)$ has been computed, we obtain a non-oscillatory polynomial piece $\widetilde{\varphi}_i(x)$ on C_i.

Remark 4.1 The HR is quite computationally expensive. To substantially reduce the overall computational cost, one can utilize a smoothness detector to turn off the HR in smooth regions. In all of the numerical simulations reported below, we have used the same low cost smoothness detector as in [7] and [20].

4.2 Remainder Correction Technique

As any of the existing high-order limiting techniques, the HR is capable of limiting the spurious oscillations, which unfortunately cannot be completely eliminated, especially in the most demanding shallow water models containing nonconservative source terms appearing on the RHS of (3.3) in the case of discontinuous bottom topography function B. Here, we introduce a technique to further regulate the remainder term $\widetilde{R}_{m,i}(x)$ in Step 1(c) of Algorithm 4.1. This technique does not affect its approximation order of accuracy and further reduces possible overshoots/undershoots near discontinuities.

In this paper, we will only consider the third-order HR. Let $\widetilde{R}_{m,i}(x) = \alpha_{m,i}(x - x_i)^2$ (with $m = 1, d = 2$). Obviously, $\widetilde{R}_{m,i}(x) = \mathcal{O}((\Delta x)^2)$ in C_i, where Δx is the spatial grid size. Based on $\widetilde{R}_{m,i}$, we want to construct a corrected remainder $\widetilde{R}^{\rm corr}_{m,i}$ satisfying the following two conditions:

$$\begin{cases} \widetilde{R}^{\rm corr}_{m,i}(x) = \widetilde{R}_{m,i}(x) + \mathcal{O}((\Delta x)^3), \quad \forall x \in C_i, \\ |\widetilde{R}^{\rm corr}_{m,i}(x)| < M, \quad \forall x \in \mathbb{R}, \text{ for some constant } M. \end{cases} \tag{4.1}$$

The first requirement in (4.1) is needed to avoid any loss of accuracy. The second condition in (4.1) is introduced to control the spurious oscillations, because $\widetilde{R}_{m,i}$ grows quite fast away from x_i and the values $\widetilde{R}_{m,i}(x_{i\pm\frac{1}{2}})$ used in Step 1(d) of Algorithm 4.1 may lead to oscillations. There are many different ways to ensure (4.1). In this paper, we take

$$\widetilde{R}^{\rm corr}_{m,i}(x) = \frac{\widetilde{R}_{m,i}(x)}{1 + \sqrt{|\alpha_{m,i}|}\,|x - x_i| + |\alpha_{m,i}|(x - x_i)^2}. \tag{4.2}$$

Theorem 4.1 *The corrected remainder* $\widetilde{R}^{\rm corr}_{m,i}$ *given by* (4.2) *satisfies the two conditions in* (4.1).

Proof: The definition of $\widetilde{R}^{\rm corr}_{m,i}$, (4.2), and the fact that $\widetilde{R}_{m,i}(x) = \mathcal{O}((\Delta x)^2)$ in C_i imply that the first condition in (4.1) holds, namely:

$$\begin{aligned} \widetilde{R}^{\rm corr}_{m,i}(x) &= \widetilde{R}_{m,i}(x)\left[1 + \mathcal{O}\Big(\sqrt{|\alpha_{m,i}|}\,|x - x_i| + |\alpha_{m,i}|(x - x_i)^2\Big)\right] = \widetilde{R}_{m,i}(x)\left[1 + \mathcal{O}\left(\Delta x + (\Delta x)^2\right)\right] \\ &= \widetilde{R}_{m,i}(x) + \mathcal{O}((\Delta x)^3), \quad \forall x \in C_i. \end{aligned}$$

The second condition in (4.1) holds because $\widetilde{R}^{\rm corr}_{m,i}$ is continuous and

$$\lim_{|x|\to\infty} \widetilde{R}^{\rm corr}_{m,i}(x) = \lim_{|x|\to\infty} \frac{\alpha_{m,i}(x - x_i)^2}{1 + \sqrt{|\alpha_{m,i}|}\,|x - x_i| + |\alpha_{m,i}|(x - x_i)^2} = \mathrm{sgn}(\alpha_{m,i}) = \pm 1.$$

■

Remark 4.2 The remainder correction technique presented in this section can be extended to higher-order HR by increasing the degree of the polynomial in the denominator on the RHS of (4.2).

Remark 4.3 In the HR process presented in Algorithm 4.1 one has to compute cell averages. This can be done analytically when the averaged quantities are polynomials. However, for other functions, for example, for the corrected remainder (4.2), it may be not easy or even impossible to evaluate the integral exactly. In such case, we replace a required cell average (except for updating the 0th degree coefficient for conservation purpose) by the average of three point-values (two end points and the center of the cell in 1D), which will not reduce the accuracy of the HR process as long as both the old polynomial and the new one are averaged in the same manner (see [39] for more details). In 2D simulations, the original HR [20] is used which works sufficiently well.

5 One-Dimensional Numerical Examples

In this section, we demonstrate performance of the well-balanced CSOC with the HR limiter. We use the third-order schemes though higher-order well-balanced CSOC can also be constructed. In all of the examples, we take the CFL number 0.4 and the gravitational acceleration constant $g = 9.812$.

Example 5.1 (Verification of the Well-Balanced Property) This test problem is taken from [36]. The computational domain is $0 \le x \le 10$, and the initial condition is the "lake at rest" state with $w(x,0) \equiv 10$, $(hu)(x,0) \equiv 0$, which should be exactly preserved. We use absorbing boundary conditions and test two different bottom topography functions. The first one is smooth:

$$B(x) = 5e^{-\frac{2}{5}(x-5)^2},$$

while the second one is nonsmooth:

$$B(x) = \begin{cases} 4, & \text{if } 4 \le x \le 8, \\ 0, & \text{otherwise.} \end{cases}$$

We use $N = 200$ uniform cells, and obtain that even at large final times both the L^1- and L^∞-errors are machine zeros for both smooth and nonsmooth bottom topographies.

Example 5.2 (Accuracy Test) The goal of this numerical example, taken [36], is to experimentally verify the order of accuracy of the (formally) third-order CSOC. The computational domain is $0 \le x \le 1$ and the boundary conditions are periodic. The initial data and bottom topography are

$$w(x,0) = 5.5 - 0.5\cos(2\pi x) + e^{\cos(2\pi x)}, \quad (hu)(x,0) = \sin(\cos(2\pi x)), \quad B(x) = \sin^2(\pi x).$$

We compute the solution of this initial-boundary value problem up to time $t = 0.1$ when the solution is still smooth (shocks will be developed at a later time). Since we use the smoothness detector mentioned in Remark 4.1, the HR limiter is essentially turned off for this smooth solution.

Since the exact solution is not available, we use Aitken's formula [1] to estimate the experimental order of accuracy r:

$$r=\log_2\left(\frac{\|u_{\frac{\Delta x}{2}}-u_{\Delta x}\|}{\|u_{\frac{\Delta x}{4}}-u_{\frac{\Delta x}{2}}\|}\right),$$

where $u_{\Delta x}$ denotes the numerical solution computed using the uniform grid of size Δx. In Table 5.1, we show the experimental orders of accuracy measured in the L^1- and L^∞-norms. As one can clearly see, the expected third order of accuracy is reached for both w and hu.

Δx	w		hu	
	L^1-order	L^∞-order	L^1-order	L^∞-order
1/50	2.3671	1.5893	1.7588	1.1060
1/100	2.4040	1.8154	2.5282	1.8850
1/200	2.8303	2.3321	2.8365	2.3537
1/400	2.9355	2.7597	2.9361	2.7652
1/800	2.9880	2.9796	2.9885	2.9729
1/1600	2.9982	2.9942	2.9982	2.9943

Table 5.1: Example 5.2: Experimental orders of accuracy.

Example 5.3 (Tidal Wave Flow) This example is taken from [3] and [36]. The computational domain is $0\le x\le L$ with $L=14000$, the initial data are

$$w(x,0)\equiv 60.5,\quad (hu)(x,0)\equiv 0,$$

the bottom topography is given by

$$B(x)=10+\frac{40x}{L}+10\,\sin\Big(\frac{4\pi x}{L}-\frac{\pi}{2}\Big),$$

and the boundary conditions are

$$w(0,t)=64.5-4\,\sin\Big(\frac{4\pi t}{86400}+\frac{\pi}{2}\Big),\quad (hu)(L,t)=0.$$

This is a good test problem since a very accurate asymptotic approximation of the exact solution was obtained in [3]:

$$w(x,t)=64.5-4\,\sin\Big(\frac{4\pi t}{86400}+\frac{\pi}{2}\Big),\quad (hu)(x,t)=\frac{\pi(x-L)}{5400}\,\cos\Big(\frac{4\pi t}{86400}+\frac{\pi}{2}\Big).\tag{5.1}$$

We compute the numerical solution at time $t=7552.13$ using 200 uniform cells and compare the obtained results with (5.1). As one can see in Figure 5.1, the numerical and analytic approximate solutions are in a very good agreement.

Example 5.4 (Perturbations of the "Lake at Rest" Steady State) This example is a slightly modified test problem, proposed in [17], which was designed to verify the ability of tested scheme

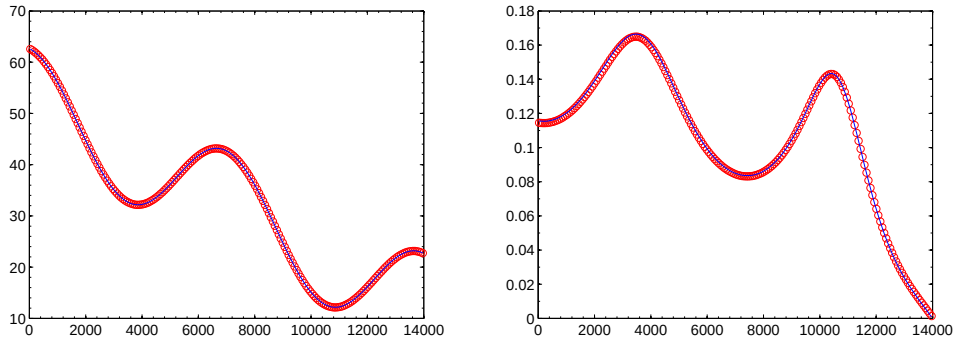

Figure 5.1: Example 5.3: Numerical (circles) and analytic (solid line) approximate solutions (h is on the left, u is on the right).

to accurately capture quasi steady-state solutions. The computational domain is $0 \le x \le 2$, and the initial data are

$$(hu)(x,0) \equiv 0, \quad w(x,0) = \begin{cases} 1+\varepsilon, & \text{if } 1.1 \le x \le 1.2, \\ 1, & \text{otherwise,} \end{cases}$$

where ε is a small perturbation constant. We use absorbing boundary conditions and consider both large ($\varepsilon = 0.2$) and small ($\epsilon = 0.001$) perturbations. The bottom topography contains a hump and is given by

$$B(x) = \begin{cases} 0.25\left[\cos(10\pi(x-1.5))+1\right], & \text{if } 1.4 \le x \le 1.6, \\ 0, & \text{otherwise.} \end{cases}$$

In this setting, the small perturbation of size ε will split into two waves, one of which will propagate to the left, while the other one will move to the right. The final time is set to be $t = 0.2$, by which the right-going wave has already passed the bottom hump. It is well-known (see, e.g., [15, 17, 36]) that when ε is small, non-well-balanced schemes cannot capture the right-going wave without producing large magnitude artificial (nonphysical) waves unless an extremely fine mesh is used.

We compute the numerical solution by both the well-balanced and non-well-balanced CSOC on a 200 uniform grid and compare the obtained results with the reference numerical solution computed using 3000 uniform cells. (The non-well-balanced CSOC is obtained by a direct application of the CSOC to the original Saint-Venant sysem (1.1) rather than to its modified version (3.3).) The results for $\varepsilon = 0.2$ and $\varepsilon = 0.001$ are shown in Figures 5.2 and Figure 5.3, respectively. As one can see there, when $\varepsilon = 0.2$ (relatively large perturbation), there is no significant difference between the solutions computed by the well-balanced and non-well-balanced CSOC. On the contrary, when $\varepsilon = 0.001$ (much smaller perturbation), the non-well-balanced CSOC generates significant artificial waves, while the well-balanced CSOC leads to a quite accurate non-oscillatory solution.

Example 5.5 (Dam Break over a Discontinuous Bottom) This problem is taken from [35] and [36] to simulate a fast changing flow over a nonsmooth bottom. The computational domain

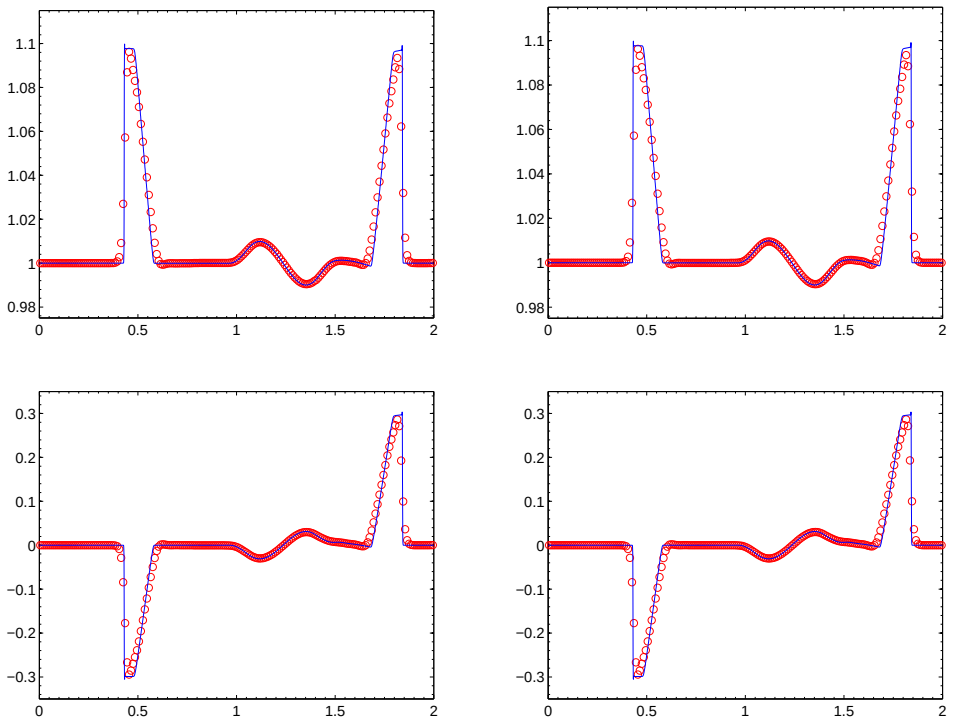

Figure 5.2: Example 5.4: $\varepsilon = 0.2$ (relatively large perturbation). Solutions (w in the top row, hu in the bottom row) computed by the non-well-balanced (left column) and well-balance (right column) CSOC using uniform grids with 200 (circles) and 3000 (solid line, reference solution) cells.

is $0 \le x \le 1500$, the initial data are

$$(hu)(x,0) \equiv 0, \quad w(x,0) = \begin{cases} 20, & \text{if } x \le 750, \\ 15, & \text{otherwise}, \end{cases}$$

and absorbing boundary conditions are used at both ends of the computational domain. The bottom topography contains a rectangular bump and is given by

$$B(x) = \begin{cases} 8, & \text{if } 562.5 \le x \le 937.5, \\ 0, & \text{otherwise}. \end{cases}$$

We compute the numerical solutions using 500 and 5000 uniform cells at two different final times: $t = 15$ (Figure 5.4) and $t = 55$ (Figure 5.5). As one can clearly see, the obtained results are very accurate and practically oscillation-free.

Remark 5.1 In this problem, the bottom topography B is a discontinuous step function, which needs to be treated carefully due to the appearance of the Dirac delta function in the source term $g[\overline{w}(t) - w]B_x$. We follow the approach in [16] and replace B in this example with its continuous piecewise linear approximation in the vicinity of jump discontinuities,

$$\widetilde{B}(x) = B_{i-\frac{1}{2}} + (B_{i+\frac{1}{2}} - B_{i-\frac{1}{2}}) \cdot \frac{x - x_{i-\frac{1}{2}}}{\Delta x}, \quad \forall x \in C_i,$$

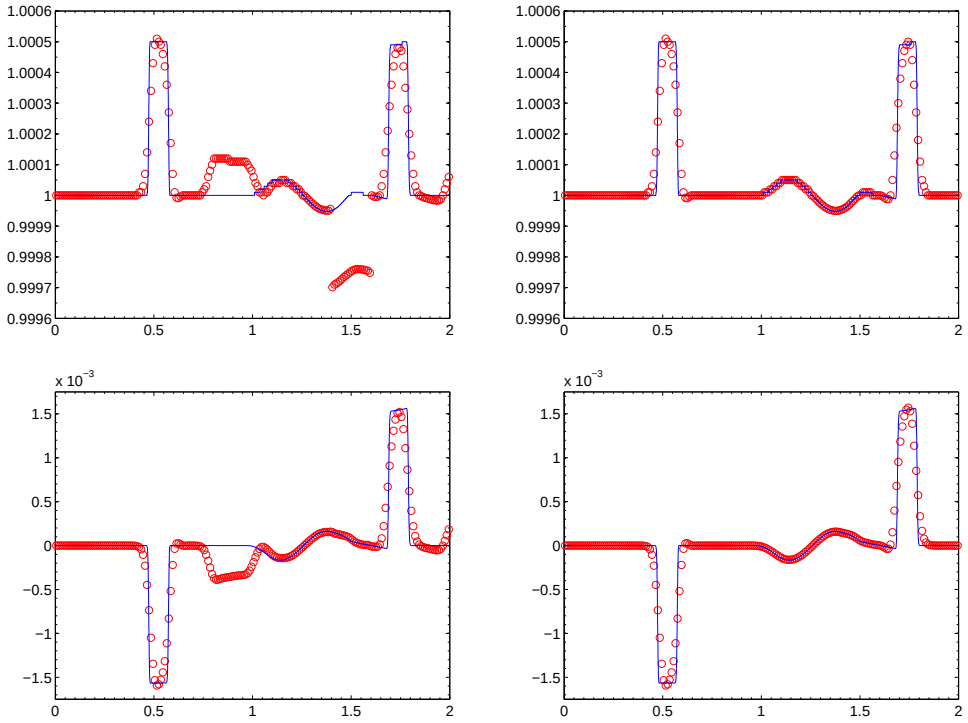

Figure 5.3: Example 5.4: $\varepsilon = 0.001$ (smaller perturbation). Solutions (w in the top row, hu in the bottom row) computed by the non-well-balanced (left column) and well-balanced (right column) CSOC using uniform grids with 200 (circles) and 3000 (solid line, reference solution) cells.

for any cell C_i in the vicinity of discontinuities, where

$$B_{i+\frac{1}{2}} := \frac{B(x_{i+\frac{1}{2}}+0)+B(x_{i+\frac{1}{2}}-0)}{2}.$$

Notice that $\widetilde{B} \to B$ as $\Delta x \to 0$.

Example 5.6 (Saint-Venant System with Manning's Friction) In this example, we consider the 1-D Saint-Venant system with Manning's friction term (see, e.g., [9, 35]):

$$\begin{cases} h_t + (hu)_x = 0, \\ (hu)_t + \left(hu^2 + \dfrac{1}{2}gh^2\right)_x = -ghB_x - g\dfrac{M^2}{h^{1/3}}u|u|, \end{cases} \tag{5.2}$$

where $M = M(x)$ is a given Manning's friction coefficient.

We note that in addition to the "lake at rest" steady states, the system (5.2) admits another physically relevant set of steady-state solutions corresponding to the water flowing down a slanted surface of a constant slope (see, e.g., [4–6]). However, in this paper, we only consider the "lake at rest" steady states and therefore, the equilibrium variables are the same as for the original Saint-Venant system (1.1), namely, $\boldsymbol{a} := (w, hu)^T$.

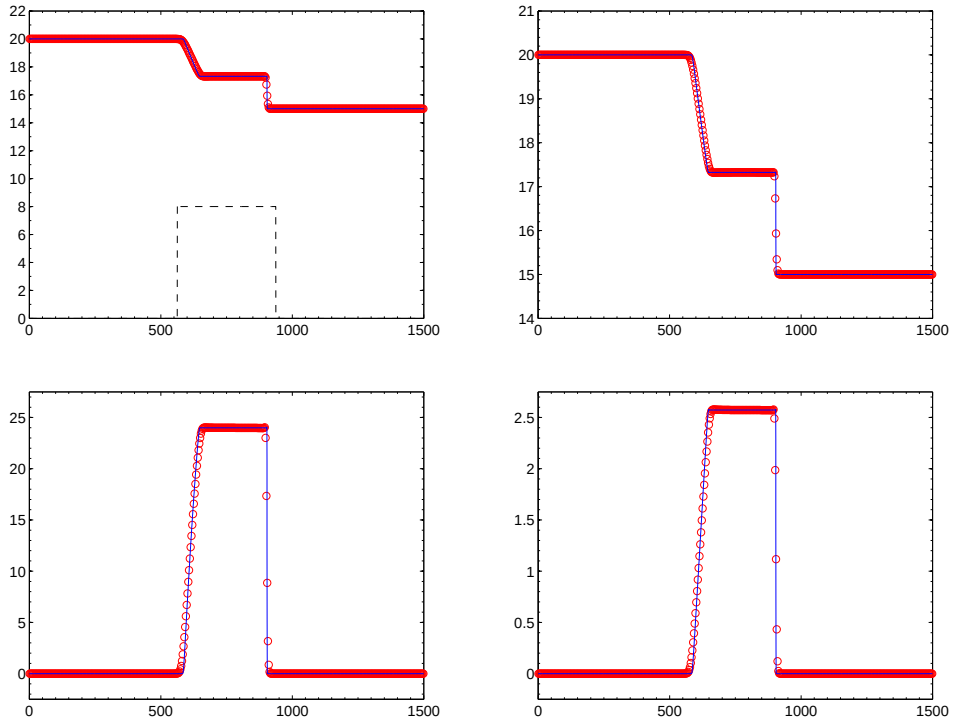

Figure 5.4: Example 5.5: $w(x,15)$ together with $B(x)$ (top left), $w(x,15)$ (top right), $hu(x,15)$ (bottom left) and $u(x,15)$ (bottom right), computed using uniform grids with 500 (circles) and 5000 (solid line) cells. The bottom topography B is plotted with the dashed line.

We now apply Algorithm 3.1 and rewrite the system (5.2) as

$$\begin{cases} w_t + (hu)_x = 0, \\ (hu)_t + \left(\dfrac{(hu)^2}{w-B} + g[\overline{w}(t)-w]B + \dfrac{g}{2}w^2\right)_x = g[\overline{w}(t)-w]B_x - g\dfrac{M^2(hu)|hu|}{(w-B)^{7/3}}, \end{cases} \tag{5.3}$$

and obtain a well-balanced scheme by a direct application of the CSOC to (5.3). To illustrate the performance of the resulting scheme, we follow [35] and consider the same setting as in Example 5.5, but with Manning's friction term with $M(x) \equiv 0.1$. The solutions computed at times $t = 15$ and $t = 55$ are shown in Figures 5.6 and 5.7, respectively. As one can clearly see, the obtained results are well-resolved and almost non-oscillatory, and the coarse and fine grid solutions are in a very good agreement.

We would like to point out that Manning's friction is only a damping term which does not smear the discontinuities. Compared with the numerical results in Example 5.5, one can see that the effect of Manning's friction is that the original horizontal line above the bump becomes oblique and the velocity magnitude decreases, which are typical effects of a damping term. Our results are in good agreements with the results reported in [35], where exactly the same phenomenon has been observed.

Example 5.7 (Steady Flows over a Hump) In this example, we study steady states with the nonzero discharge hu. The properties of such flows depend on the bottom topography and free-

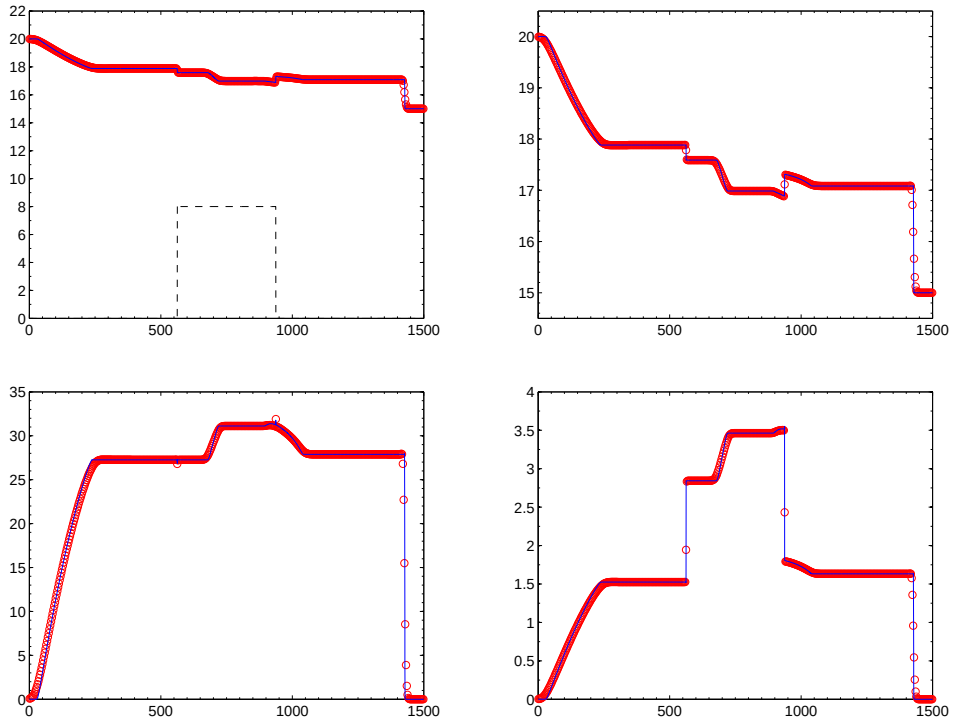

Figure 5.5: Example 5.5: $w(x,55)$ together with $B(x)$ (top left), $w(x,55)$ (top right), $hu(x,55)$ (bottom left) and $u(x,55)$ (bottom right), computed using uniform grids with 500 (circles) and 5000 (solid line) cells. The bottom topography B is plotted with the dashed line.

stream Froude number $Fr = u/\sqrt{gh}$. If $Fr < 1$ (subcritical flow) or $Fr > 1$ (supercritical flow) everywhere, then the steady-state solution will be smooth. Otherwise, the flow is transcritical with transitions at the points where Fr passes through 1, and thus one of the eigenvalues $u \pm \sqrt{gh}$ of the Jacobian matrix passes through zero. In such case, the steady-state solution may contain a stationary shock. Steady flows over a hump are classical benchmarks for transcritical and subcritical steady flows, and are widely used to test numerical schemes for the shallow water system, see, for example, [15, 17, 34, 36].

The computational domain is $0 \le x \le 25$, and the initial data are

$$w(x,0) \equiv 0.5, \quad (hu)(x,0) \equiv 0.$$

The bottom topography contains a hump and is given by

$$B(x) = \begin{cases} 0.2 - 0.05(x-10)^2, & \text{if } 8 \le x \le 12, \\ 0, & \text{otherwise.} \end{cases}$$

The nature of the solution depends on the boundary condition: The flow can be subcritical or transcritical with or without a stationary shock. The final time is set to be $t = 200$ by which all of the solutions reach their corresponding steady states.

Case 1: Subcritical Flow.

We set the following upstream and downstream boundary conditions: $(hu)(0,t) = 4.42$ and $w(25,t) = 2$. In Figure 5.8 (left), we plot the obtained Froude number Fr, which gradually

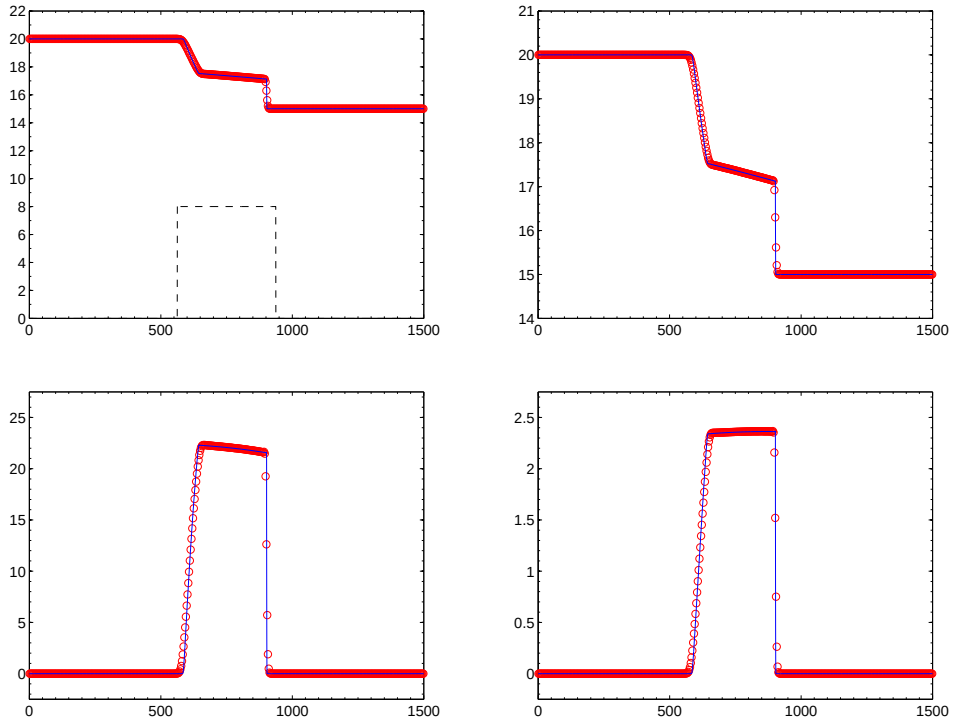

Figure 5.6: Example 5.6: $w(x,15)$ together with $B(x)$ (top left), $w(x,15)$ (top right), $hu(x,15)$ (bottom left) and $u(x,15)$ (bottom right), computed using uniform grids with 500 (circles) and 5000 (solid line) cells. The bottom topography B is plotted with the dashed line.

increases to a large (but still smaller than 1) value above the hump and then gradually decreases back to the original value. We compute the numerical solutions using 100 and 1000 uniform cells. As it can be seen in Figure 5.9, the obtained solutions are in good agreement and both are non-oscillatory.

Case 2: Transcritical Flow without a Stationary Shock.

We now take different upstream and downstream boundary conditions: $(hu)(0,t) = 1.53$ and $w(25,t) = 0.41$. In Figure 5.8 (middle), we plot the obtained Froude number Fr, which now gradually increases to a value greater than 1 above the hump and then remains constant. Therefore, no stationary shocks appear on the surface. We compute the numerical solutions using 200 and 2000 uniform cells. As in the subcritical case, the coarse and fine grid solutions are in a good agreement and both are practically non-oscillatory, see Figure 5.10.

Case 3: Transcritical Flow with a Stationary Shock.

In this case, the upstream and downstream boundary conditions are $(hu)(0,t) = 0.18$ and $w(25,t) = 0.33$. The obtained Froude number Fr is plotted in Figure 5.8 (right). As in the previous case, the Froude number gradually increases to a value greater than 1 above the hump, but then it jumps down to the value much smaller than 1. Therefore, a stationary shock appears on the surface. We compute the numerical solutions, presented in Figure 5.11, using 100 and 1000 uniform cells. As in Cases 1 and 2, both solutions are almost non-oscillatory and in a good agreement, and the stationary shock wave is sharply resolved.

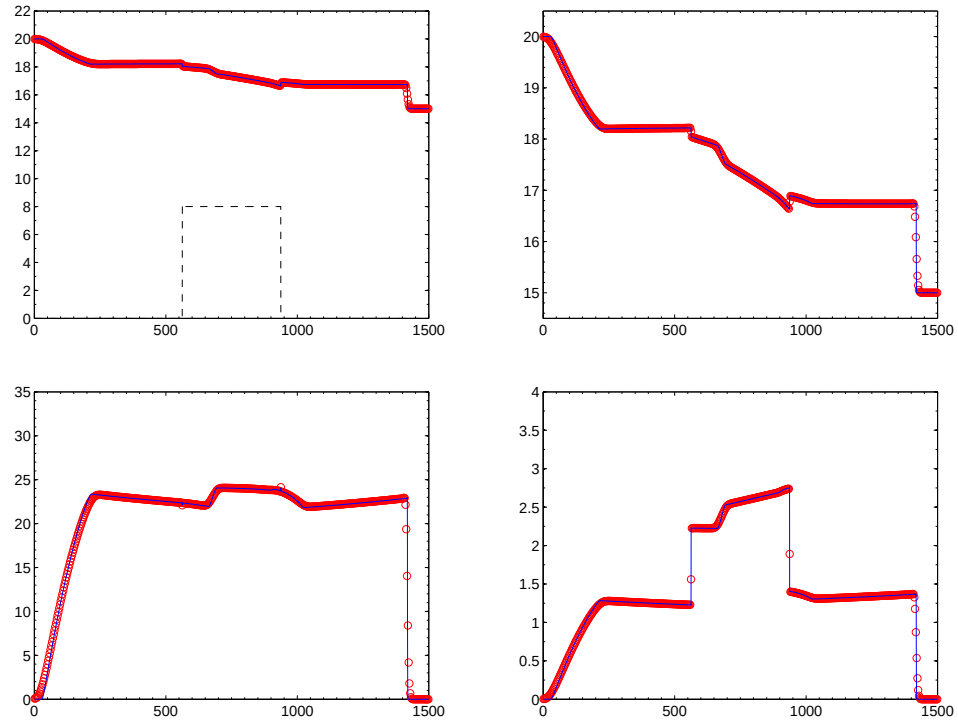

Figure 5.7: Example 5.6: $w(x,55)$ together with $B(x)$ (top left), $w(x,55)$ (top right), $hu(x,55)$ (bottom left) and $u(x,55)$ (bottom right), computed using uniform grids with 500 (circles) and 5000 (solid line) cells. The bottom topography B is plotted with the dashed line.

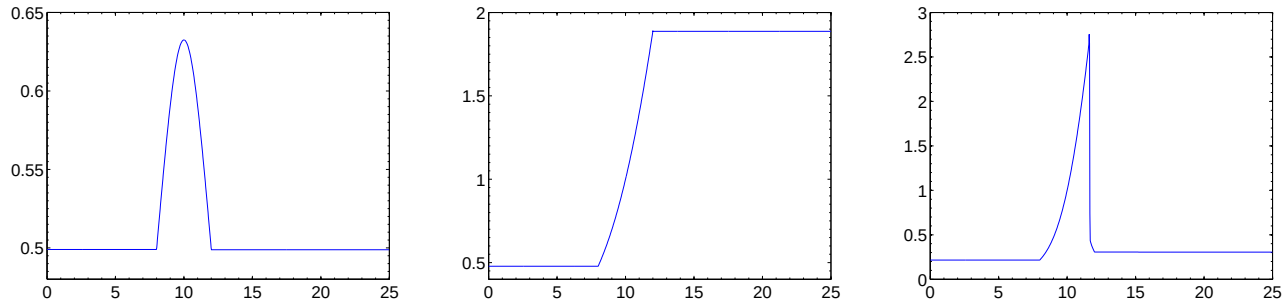

Figure 5.8: Example 5.7: Froude number Fr of the steady flows over a hump in the subcritical (left), transcritical without a stationary shock (middle) and transcritical with a stationary shock (right) cases.

6 Two-Dimensional Numerical Examples

In this section, we consider the 2-D Saint-Venant system (1.2), for which "lake at rest" steady-state solutions are given by (1.3) and the corresponding equilibrium variables are $\boldsymbol{a} := (w, hu, hv)^T$. When written in terms of $\boldsymbol{a}$, the source term becomes $\boldsymbol{S} = \big(0, -g(w-B)B_x, -g(w-B)B_y\big)^T$.

Let $\overline{w}(t)$ be the global spatial average of the water surface $w(x,y,t)$. We now apply the constant

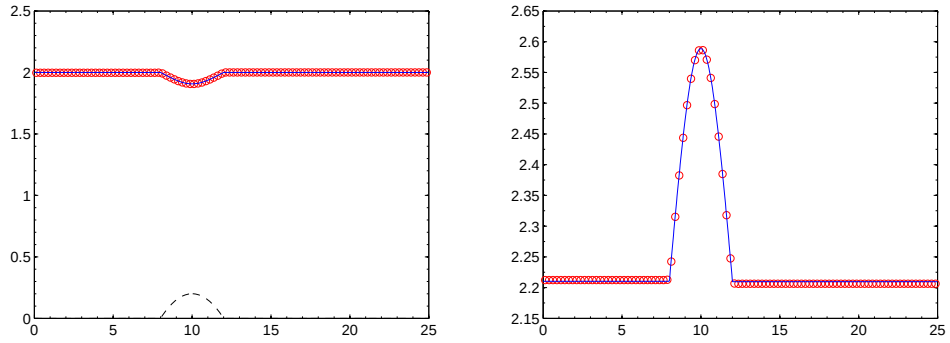

Figure 5.9: Example 5.7, subcritical case: Solutions (w together with B is on the left, u is on the right) computed using uniform grids with 100 (circles) and 1000 (solid line) cells. The bottom topography B is plotted with the dashed line.

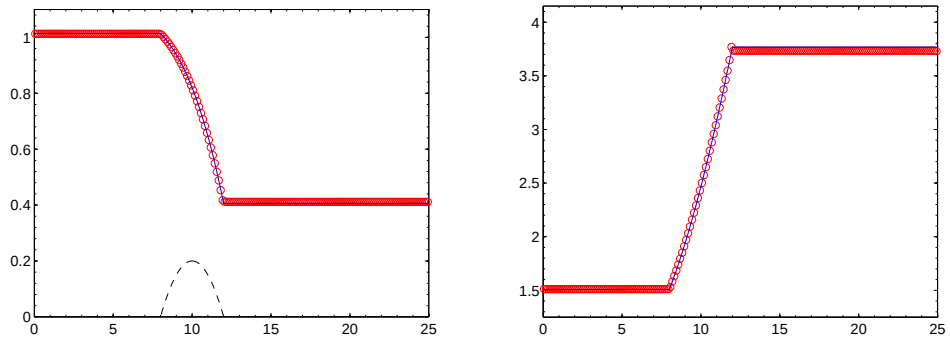

Figure 5.10: Example 5.7, transcritical case without a stationary shock: Solutions (w together with B is on the left, u is on the right) computed using uniform grids with 200 (circles) and 2000 (solid line) cells. The bottom topography B is plotted with the dashed line.

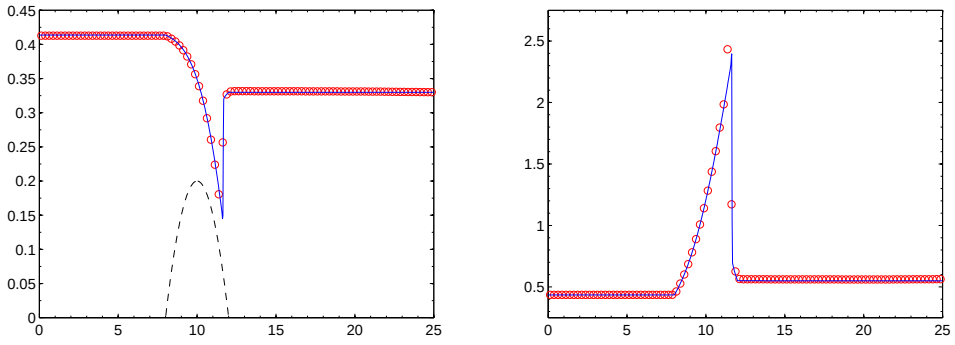

Figure 5.11: Example 5.7, transcritical case with a stationary shock: Solutions (w together with B is on the left, u is on the right) computed using uniform grids with 100 (circles) and 1000 (solid line) cells. The bottom topography B is plotted with the dashed line.

subtraction technique presented in Section 3 to the system (1.2) and rewrite it as

$$\begin{cases} w_t + (hu)_x + (hv)_y = 0, \\ (hu)_t + \left(\dfrac{(hu)^2}{w-B} + g[\overline{w}(t)-w]B + \dfrac{g}{2}w^2\right)_x + \left(\dfrac{(hu)(hv)}{w-B}\right)_y = g[\overline{w}(t)-w]B_x, \\ (hv)_t + \left(\dfrac{(hu)(hv)}{w-B}\right)_x + \left(\dfrac{(hv)^2}{w-B} + g[\overline{w}(t)-w]B + \dfrac{g}{2}w^2\right)_y = g[\overline{w}(t)-w]B_y. \end{cases} \tag{6.1}$$

The system (6.1) is advantageous over the original system (1.2) since at "lake at rest" steady states, the source terms in the system (6.1) vanish and the fluxes are constant. Therefore, a direct application of the CSOC from [18] leads to the 2-D well-balanced CSOC.

As in the 1-D case, all of the simulations in this section are conducted by the third-order well-balanced CSOC with the HR limiter. In all of the 2-D examples, we take the CFL number 0.45 and the gravitational acceleration constant $g = 9.812$.

Example 6.1 (Verification of the Well-Balanced Property) This test problem is taken from [36]. The computational domain is $[0,1]\times[0,1]$, and the initial condition is the "lake at rest" state with $w(x,y,0)\equiv 1$, $(hu)(x,y,0)\equiv(hv)(x,y,0)\equiv 0$ and $B(x,y)=0.8e^{-50[(x-0.5)^2+(y-0.5)^2]}$, which should be exactly preserved. We use absorbing boundary conditions and compute the numerical solution at time $t=0.1$ using a 100×100 uniform mesh. The L^1- and L^∞-errors for both the surface level w and discharges hu and hv are shown in Table 6.1. As one can see, the L^1-errors are machine zeros, while the L^∞-errors are also very close to the round-off errors and are smaller than the errors reported in [36].

	w	hu	hv
L^1-error	2.2160×10^{-17}	8.4091×10^{-18}	9.5723×10^{-18}
L^∞-error	8.6597×10^{-15}	3.9053×10^{-15}	4.4746×10^{-15}

Table 6.1: Example 6.1: L^1- and L^∞-errors at time $t=0.1$.

We have also computed a long time solution of this problem and observed that the L^1-errors remain equal to machine zeros.

Example 6.2 (Small Perturbation of the "Lake at Rest" State) This test problem, proposed in [17], is a 2-D version of Example 5.4. The computational domain is $[0,2]\times[0,1]$, the initial data are

$$(hu)(x,y,0)\equiv(hv)(x,y,0)\equiv 0,\quad w(x,y,0)=\begin{cases}1.01, & \text{if } 0.05\le x\le 0.15,\\ 1, & \text{otherwise.}\end{cases}$$

and absorbing boundary conditions are imposed at all of the boundaries. The bottom topography contains a vertical hump is given by

$$B(x,y)=0.8e^{-5(x-0.9)^2-50(y-0.5)^2}.$$

We compute the solution and monitor how the right-going disturbance propagates past the hump (the left-going disturbance leaves the domain and does not affect the solution after this). We use two uniform grids with 200×100 and 600×300 cells. The snapshots of the computed solution at times $t=0.12, 0.24, 0.36, 0.48$ and 0.6 are shown in Figure 6.1. Notice that the wave speed is smaller above the hump than anywhere else, which distorts the initially planar disturbance. The obtained results clearly demonstrate that the CSOC can capture the small perturbation and resolve the complicated features of the studied flow very well.

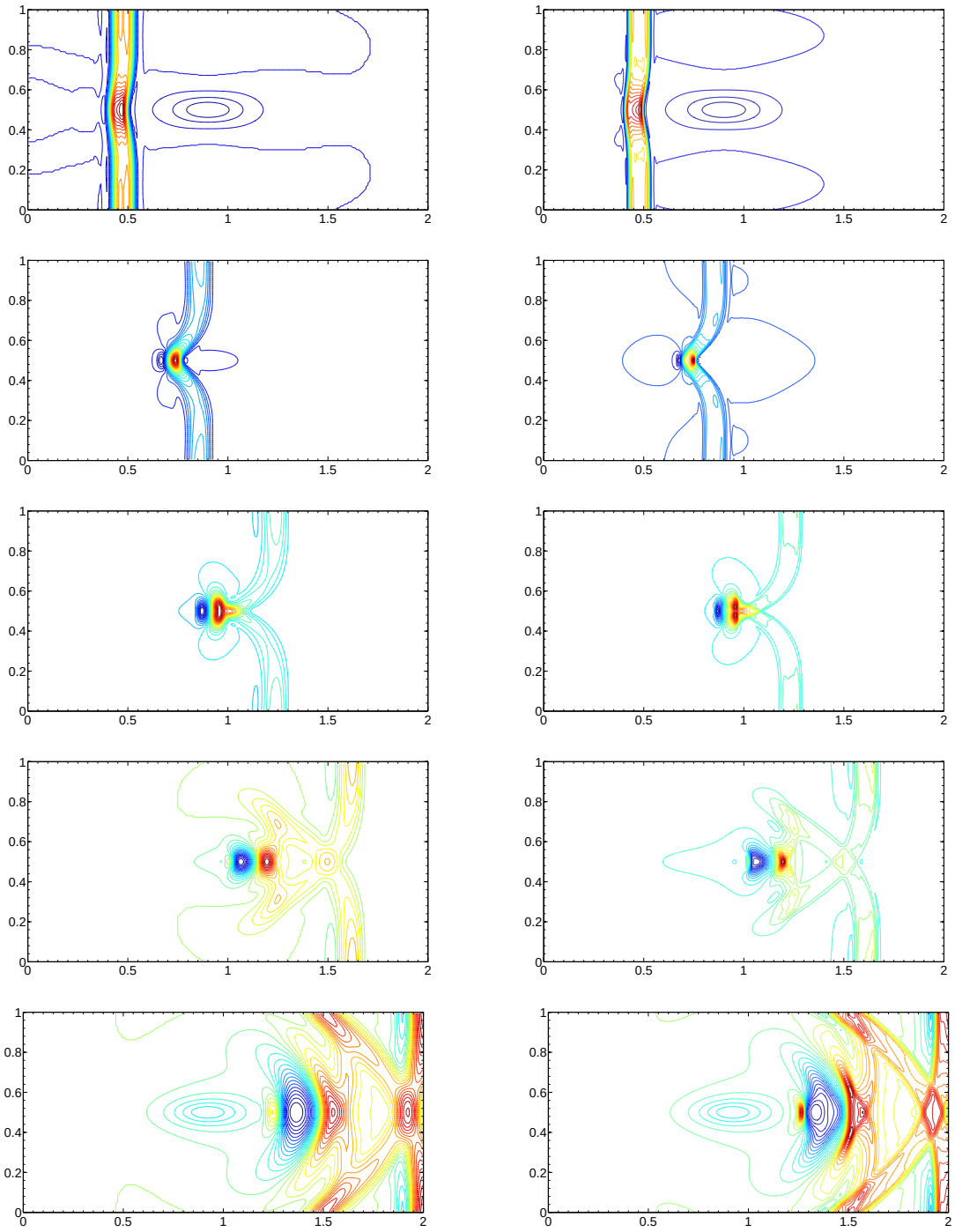

Figure 6.1: Example 6.2: Contour-plot of w on 200×100 (left) and 600×300 (right) uniform meshes. The solution is shown at times $t = 0.12, 0.24, 0.36, 0.48, 0.6$ (from top to bottom).

7 Conclusions and Future Works

In this paper, we have developed central schemes on overlapping cells (CSOC) for the Saint-Venant system of shallow water equations in both one and two space dimensions. A new constant subtraction technique is proposed to make the CSOC well-balanced, that is, to guarantee that

they exactly preserve "lake at rest" steady states while still maintain the original high-order of accuracy and non-oscillatory property. In fact, this technique is quite general and can be utilized for development other finite-volume schemes (this will be done in our future works). We have provided extensive numerical results to demonstrate the well-balanced property, high-order of accuracy and non-oscillatory nature of the proposed CSOC. Our future works will include development of positivity-preserving CSOC and also extension of their well-balanced properties to the case of more general steady-state solutions.

References

[1] K. E. Atkinson, An introduction to numerical analysis, *John Wiley & Sons Inc., New York, second ed.*, 1989.

[2] E. Audusse, F. Bouchut, M.-O. Bristeau, R. Klein and B. Perthame, A fast and stable well-balanced scheme with hydrostatic reconstruction for shallow water flows, *SIAM J. Sci. Comput.*, 25 (2004), 2050–2065.

[3] A. Bermudez and M. E. Vazquez, Upwind methods for hyperbolic conservation laws with source terms, *Comput. & Fluids*, 23 (1994), 1049–1071.

[4] L. Cea, M. Garrido and J. Puertas, Experimental validation of two-dimensional depth-averaged models for forecasting rainfall-runoff from precipitation data in urban areas, *J. Hydrol.*, 382 (2010), 88–102.

[5] L. Cea and M. E. Vázquez-Cendón, Unstructured finite volume discretisation of bed friction and convective flux in solute transport models linked to the shallow water equations, *J. Comput. Phys.*, 231 (2012), 3317–3339.

[6] A. Chertock, S. Cui, A. Kurganov and T. Wu, Well-balanced positivity preserving central-upwind scheme for the shallow water system with friction terms, *Internat. J. Numer. Meth. Fluids*, Submitted.

[7] N. Chevaugeon, J. Xin, P. Hu, X. Li, D. Cler, J. E. Flaherty and M. S. Shephard, Discontinuous Galerkin methods applied to shock and blast problems, *J. Sci. Comput.*, 22/23 (2005), 227–243.

[8] A. de Saint-Venant, Thèorie du mouvement non-permanent des eaux, avec application aux crues des rivière at à l'introduction des marèes dans leur lit., *C.R. Acad. Sci. Paris*, 73 (1871), 147–154.

[9] A. Flamant, Mécanique appliquée : Hydraulique, *Baudry éditeur, Paris (France)*, 1891.

[10] T. Gallouët, J.-M. Hérard and N. Seguin, Some approximate Godunov schemes to compute shallow-water equations with topography, *Comput. & Fluids*, 32 (2003), 479–513.

[11] S. Gottlieb, D. Ketcheson and C.-W. Shu, Strong stability preserving Runge-Kutta and multistep time discretizations, *World Scientific Publishing Co. Pte. Ltd., Hackensack, NJ*, 2011.

[12] S. Gottlieb, C.-W. Shu and E. Tadmor, Strong stability-preserving high-order time discretization methods, *SIAM Rev.*, 43 (2001), 89–112.

[13] A. Harten, B. Engquist, S. Osher and S. R. Chakravarthy, Uniformly high-order accurate essentially nonoscillatory schemes. III, *J. Comput. Phys.*, 71 (1987), 231–303.

[14] S. Jin, A steady-state capturing method for hyperbolic systems with geometrical source terms, *M2AN Math. Model. Numer. Anal.*, 35 (2001),631–645.

[15] A. Kurganov and D. Levy, Central-upwind schemes for the Saint-Venant system, *M2AN Math. Model. Numer. Anal.*, 36 (2002), 397–425.

[16] A. Kurganov and G. Petrova, A second-order well-balanced positivity preserving central-upwind scheme for the Saint-Venant system, *Commun. Math. Sci.*, 5 (2007), 133–160.

[17] R. J. LeVeque, Balancing source terms and flux gradients in high-resolution Godunov methods: the quasi-steady wave-propagation algorithm, *J. Comput. Phys.*, 146 (1998), 346–365.

[18] Y. Liu, Central schemes on overlapping cells, *J. Comput. Phys.*, 209 (2005), 82–104.

[19] Y. Liu, C.-W. Shu, E. Tadmor and M. Zhang, Central discontinuous Galerkin methods on overlapping cells with a nonoscillatory hierarchical reconstruction, *SIAM J. Numer. Anal.*, 45 (2007), 2442–2467.

[20] Y. Liu, C.-W. Shu, E. Tadmor and M. Zhang, Non-oscillatory hierarchical reconstruction for central and finite volume schemes, *Commun. Comput. Phys.*, 2 (2007), 933–963.

[21] M. Lukáčová-Medviďová, S. Noelle and M. Kraft, Well-balanced finite volume evolution Galerkin methods for the shallow water equations, *J. Comput. Phys.*, 221 (2007), 122–147.

[22] H. Nessyahu and E. Tadmor, Nonoscillatory central differencing for hyperbolic conservation laws, *J. Comput. Phys.*, 87 (1990), 408–463.

[23] S. Noelle, N. Pankratz, G. Puppo and J. R. Natvig, Well-balanced finite volume schemes of arbitrary order of accuracy for shallow water flows, *J. Comput. Phys.*, 213 (2006), 474–499.

[24] S. Noelle, Y. Xing and C.-W. Shu, High-order well-balanced finite volume WENO schemes for shallow water equation with moving water, *J. Comput. Phys.*, 226 (2007), 29–58.

[25] G. Russo, Central schemes for conservation laws with application to shallow water equations, in *Trends and Applications of Mathematics to Mechanics, Springer Milan*, 2005, 225-246.

[26] C.-W. Shu, Numerical experiments on the accuracy of ENO and modified ENO schemes, *J. Sci. Comput.*, 5 (1990), 127–149.

[27] C.-W. Shu, Essentially non-oscillatory and weighted essentially non-oscillatory schemes for hyperbolic conservation laws, in *Advanced numerical approximation of nonlinear hyperbolic equations (Cetraro, 1997), Lecture Notes in Math., Springer, Berlin*, 1697 (1998), 325–432.

[28] C.-W. Shu, High order weighted essentially nonoscillatory schemes for convection dominated problems, *SIAM Rev.*, 51 (2009), 82–126.

[29] C.-W. Shu and S. Osher, Efficient implementation of essentially non-oscillatory shock-capturing schemes, *J. Comput. Phys.*, 77 (1988), 439–471.

[30] C.-W. Shu and S. Osher, Efficient implementation of essentially nonoscillatory shock-capturing schemes. II, *J. Comput. Phys.*, 83 (1989), 32–78.

[31] B. van Leer, Towards the ultimate conservative difference scheme. II. Monotonicity and conservation combined in a second-order scheme, *J. Comput. Phys.*, 14 (1974), 361–370.

[32] B. van Leer, Towards the ultimate conservative difference scheme. IV. A new approach to numerical convection, *J. Comput. Phys.*, 23 (1977), 276–299.

[33] B. van Leer, Towards the ultimate conservative difference scheme. V. A second-order sequel to Godunov's method, *J. Comput. Phys.*, 32 (1979), 101–136.

[34] M. E. Vázquez-Cendón, Improved treatment of source terms in upwind schemes for the shallow water equations in channels with irregular geometry, *J. Comput. Phys.*, 148 (1999), 497–526.

[35] S. Vukovic and L. Sopta, ENO and WENO schemes with the exact conservation property for one-dimensional shallow water equations, *J. Comput. Phys.*, 179 (2002), 593–621.

[36] Y. Xing and C.-W. Shu, High order finite difference WENO schemes with the exact conservation property for the shallow water equations, *J. Comput. Phys.*, 208 (2005), 206–227.

[37] Y. Xing and C.-W. Shu, High-order well-balanced finite difference WENO schemes for a class of hyperbolic systems with source terms, *J. Sci. Comput.*, 27 (2006), 477–494.

[38] Y. Xing and C.-W. Shu, High order well-balanced finite volume WENO schemes and discontinuous Galerkin methods for a class of hyperbolic systems with source terms, *J. Comput. Phys.*, 214 (2006), 567–598.

[39] Z. Xu, Y. Liu, H. Du, G. Lin and C.-W. Shu, Point-wise hierarchical reconstruction for discontinuous Galerkin and finite volume methods for solving conservation laws *J. Comput. Phys.*, 230 (2011), 6843–6865.